aerospace

MDPI

Article

Orbital Analysis of a Dual Asteroid System Explorer Based on the Finite Element Method

Linli Su, Wenyu Feng, Lie Yang, Zichen Fan, Mingying Huo and Naiming Qi *

Department of Aerospace Engineering, Harbin Institute of Technology, Harbin 150001, China
* Correspondence: qinmok@163.com

Abstract: In the study of dual asteroid systems, a model that can rapidly compute the motion and orientation of these bodies is essential. Traditional modeling techniques, such as the double ellipsoid or polyhedron methods, fail to deliver sufficient accuracy in estimating the interactions between dual asteroids. This inadequacy primarily stems from the non-tidally locked nature of asteroid systems, which necessitates continual adjustments to account for changes in gravitational fields. This study adopts the finite element method to precisely model the dynamic interaction forces within irregular, time-varying dual asteroid systems and, thereby, enhance the planning of spacecraft trajectories. It is possible to derive the detailed characteristics of a spacecraft's orbital patterns via the real-time monitoring of spacecraft orbits and the relative positions of dual asteroids. Furthermore, this study examines the orbital stability of a spacecraft under various trajectories, revealing that orbital stability is intrinsically linked to the geometric configuration of the orbits. And considering the influence of solar pressure on the orbit of asteroid detectors, a method was proposed to characterize the stability of detector orbits in the time-varying gravitational field of binary asteroids using cloud models. The insights gained from the analysis of orbital characteristics can inform the design of landing trajectories for binary asteroid systems and provide data for deep learning algorithms that are aimed at optimizing such orbits. By introducing the application of the finite element method, detailed analysis of spacecraft orbit characteristics, and a stability characterization method based on a cloud model, this paper systematically explores the logic and structure of spacecraft orbit planning in a dual asteroid system.

Keywords: dual asteroids; finite element method; orbit; stability

check for updates

Citation: Su, L.; Feng, W.; Yang, L.; Fan, Z.; Huo, M.; Qi, N. Orbital Analysis of a Dual Asteroid System Explorer Based on the Finite Element Method. *Aerospace* **2024**, *11*, 993. https://doi.org/10.3390/aerospace11120993

Academic Editor: Mikhail Ovchinnikov

Received: 10 October 2024
Revised: 15 November 2024
Accepted: 23 November 2024
Published: 30 November 2024

Copyright: © 2024 by the authors. Licensee MDPI, Basel, Switzerland. This article is an open access article distributed under the terms and conditions of the Creative Commons Attribution (CC BY) license (https://creativecommons.org/licenses/by/4.0/).

1. Introduction

As technological advancements continue to propel the aerospace sector forward, humanity's focus is increasingly shifting toward the vast expanse of the cosmos. The study of asteroids in the solar system has emerged as a pivotal area of interest in contemporary deep space exploration. These celestial bodies were formed concurrently with the solar system and did not undergo the evolutionary processes of the planets. Thus, they preserved a wealth of materials from the early solar system. This makes asteroids repositories of relatively undisturbed information regarding the nascent stages of the formation of the solar system and offer crucial insights into its origin and early evolution. Furthermore, certain asteroids are believed to harbor rare metals and other valuable resources, meaning that they present significant opportunities for space mining. These facts have intensified the need for the enhanced detection and meticulous study of asteroids and have set higher standards for current and future space exploration missions.

The discovery of binary asteroid systems has significantly increased, marking a pivotal advancement in space exploration. In October 2021, the United States launched the Lucy probe, which achieved a milestone by detecting the binary asteroid system Ida243 and its satellite Dactyl [1]. Over the next 12 years, Lucy is slated to conduct flyby missions to study multiple Trojan asteroids, including the binary systems Eurybates 3548 and Patroclus

617. In a parallel development, November 2021 saw NASA launch the double asteroid redirection test (DART) mission, which targeted the near-Earth binary [2] asteroid system Didymos 65803. Using a kinetic impactor, the mission altered the orbit of the asteroid and, thereby, validated defense techniques against near-Earth asteroids. Additionally, NASA's Small Innovative Missions for Planetary Exploration (SIMPLEx) program approved the Janus [3] mission, which targeted the near-Earth binary asteroid systems FG3 1996 and VH 1991. Janus aimed to use a dual lightweight and cost-effective spacecraft to execute high-resolution imaging and precise modeling to delve into the formation and evolutionary mechanisms of binary systems. According to observational data, many binary asteroid systems exist in the cosmos and account for approximately 16% of the total number of near-Earth asteroids [4].

However, the proximity operations of a binary asteroid explorer are inseparable from the gravitational interactions of binary asteroids. The gravitational field in the vicinity of a binary asteroid system is intricately connected to the orientations and positions of the constituent asteroids. Therefore, studying the attitude and orbital motion of these two asteroids is crucial for understanding the gravitational field of a binary asteroid system. The attitude and orbital motion of an asteroid is determined by system dynamics. Considering that the shapes of the two asteroids are relatively complex, their volumes and masses are small, their mass distributions are uneven, and their spin rates are fast, the gravitational field distribution near the asteroids is irregular, weak, and subject to significant variations, compared to those of typical spherical planets. This complexity often leads to the dynamic behavior of binary asteroid systems manifesting as coupled attitude–orbit motion, which is a scenario that is typically described by the two-body problem in celestial mechanics. Despite the clear importance of the gravitational mutual potential in studying the kinematics of binary asteroid systems, there is generally no closed-form solution for calculating the mutual potential between two asteroids with irregular shapes and nonuniform mass distributions.

In recent decades, scholars have devoted significant efforts to developing methods for calculating the gravitational mutual potentials of binary asteroid systems. These methodologies are crucial for the preliminary study of the gravitational fields of binary asteroids during the mission planning phases of space probes. The primary focus of this study was to identify an effective approach by which to accurately describe these gravitational fields, which would lay the foundation for subsequent investigations. Currently, the most prevalent methods for modeling the gravitational field include the simple geometry model, spherical and ellipsoidal harmonic expansion model, mass group model, and homogeneous polyhedron method. Each of these modeling techniques has its own set of advantages and drawbacks in terms of generality, computational speed, accuracy, scope of application, and additional storage requirements. These factors play critical roles in determining the suitability of each method for specific applications in the study of the gravitational fields in binary asteroid systems. For example, Werner and Scheeres [5] used an infinite series to express the mutual gravitational potential between a pair of homogeneous polyhedra. Fahnestock and Scheeres [6] further investigated this work by deriving a method by which to compute the derivative of the mutual gravitational potential between two objects with arbitrary positions and attitudes. Based on these studies, Scheeres et al. [7] studied the dynamics of the near-Earth binary asteroid (66391) 1999 KW4 and performed dynamic simulations and analyses. Furthermore, Compere and Lemaıtre [8] elaborated and completed the formulation of the mutual potential between two bodies using the symmetric free trace (STF) tensor form developed by their predecessors. Moreover, Shi et al. [9] proposed a shape-based mutual gravitational potential model and used it to simulate the evolution of the asteroid (66391) 1999 KW4. Using this method, one binary asteroid is modeled as a homogeneous polyhedron, and the other is modeled as an extended rigid body with an arbitrary mass distribution. However, simple geometric models and spherical harmonic series expansions are not applicable to irregularly shaped asteroids. The mass group model is more accurate, but it often requires the discretization of the asteroid when describing its

gravitational field, which leads to a limited spatial resolution of the model. Additionally, the homogeneous polyhedron method fails to characterize the mass distribution inside the asteroid. To solve these problems, Yu et al. [10] developed a finite element method by which to calculate the gravitational interactions between two bodies of arbitrary shapes. This method is not limited by the shape or internal mass distribution of asteroids; it accurately describes the mutual gravitational potentials between two free gravitational bodies, and it effectively addresses the issue of nonconvergence, which is often encountered with traditional methods. This approach is particularly valuable for modeling the gravitational fields of binary asteroid systems that are non-tidally locked and have time-varying characteristics. This method also provides a reliable tool for understanding and predicting the dynamic behavior of binary asteroid systems, and it can accurately determine the gravitational force acting on a detector at any given time. As a result, this method enables the precise calculation of the detector's orbit around a time-varying, irregular binary asteroid system. This capability is essential for the successful navigation and study of complex celestial environments.

For space probe missions, identifying specific orbits that maintain stability for extended periods is critical because of the complex dynamics of gravitational fields around binary asteroid systems. This stability minimizes the need for frequent maneuvering and reduces the risk of the collision or loss of the spacecraft, particularly during malfunctions. Damme et al. [11] conducted numerical studies to analyze the lifespans of orbits close to celestial bodies and found that the shape of an orbit significantly influences its durability. Dell'Elce et al. [12] explored stable orbits around binary asteroids and discovered that some orbits that were previously considered to be stable, such as those at Lagrange points, become unstable under non-tidally locked conditions. These researchers used a Monte Carlo analysis to examine the survival rates of these orbits. Shang et al. [13] introduced a method for identifying Lagrangian coherent structures (LCSs) in asynchronous binary asteroid systems that represent critical dynamic pathways. More recently, Ferrari et al. [14] investigated different dynamic regions around binary asteroids and outlined advantageous trajectories by using waypoint strategies and frequent orbit adjustments. Building on this research, Naidu et al. [15] refined the physical models used in radar observations of near-Earth asteroids. This collective study provides invaluable insights for planning and conducting space missions in challenging environments.

Previous studies have primarily focused on the spherical and ellipsoidal gravitational fields of asteroids to address their irregular shapes. However, binary asteroid systems often exhibit a high degree of irregularity, which can affect the stability of an orbit. To explore how these complexities affect probe orbits, we analyzed two different sets of probe orbits within irregular, time-varying binary asteroid systems. By studying the evolution of these orbits, we tracked the changes in their velocity, semi-major axis, eccentricity, orbital inclination, right ascension of the ascending node, and arguments of the perigee. The stabilities of these orbits were compared to provide a framework for assessing the probe orbits in binary asteroid systems. This analysis provides crucial insights into the dynamic nature of orbits in environments shaped by complex gravitational interactions.

To effectively address these challenges, this paper is organized as follows: Section 2 introduces the finite element model of binary asteroids and details the computational methods for calculating gravitational interactions. Section 3 discusses the generation of probe orbits and simulates various orbital trajectories within the binary asteroid system. Section 4 provides an in-depth analysis of the probe's orbital characteristics, contrasting different models and evaluating their effectiveness. Section 5 analyzes the orbital stability using a cloud model approach, considering the impact of solar pressure, and presents a method for characterizing orbit stability. Finally, Section 6 concludes the study, summarizing the key findings and suggesting directions for future research. This logical structure ensures a coherent progression from modeling to simulation and analysis, ultimately supporting the planning and optimization of spacecraft missions in dual asteroid environments.

2. Binary Asteroid Model

To select a model for the binary asteroids, we drew on the work of Scheeres et al. [6], who studied the dynamics of near-Earth binary asteroids. Their approach involved calculating mutual gravitational potentials by using the uniform polyhedron method [16] and analyzing the gravitational interactions and derivatives with bilinear tetrahedral elements for the two-body problem [17]. Based on this foundational research, a finite element model was developed, and a dynamic simulation of the 1999 KW4 binary asteroid system was conducted. This method provides a comprehensive framework for understanding the complex interactions within binary asteroid systems.

2.1. Finite Element Model of Binary Asteroids

The primary goal of using the finite element method in this study was to compute the gravitational interactions between two bodies, which are designated as rigid bodies A and B. To address the two-body problem, this approach models both bodies as compositions of tetrahedral elements. This method utilizes three coordinate systems: the world coordinate system (W) and two systems, namely A and B, which are rigidly attached to bodies A and B, respectively. Figure 1 shows the definitions and relationships of these coordinate systems. This setup provides a clear and organized framework for analyzing gravitational forces.

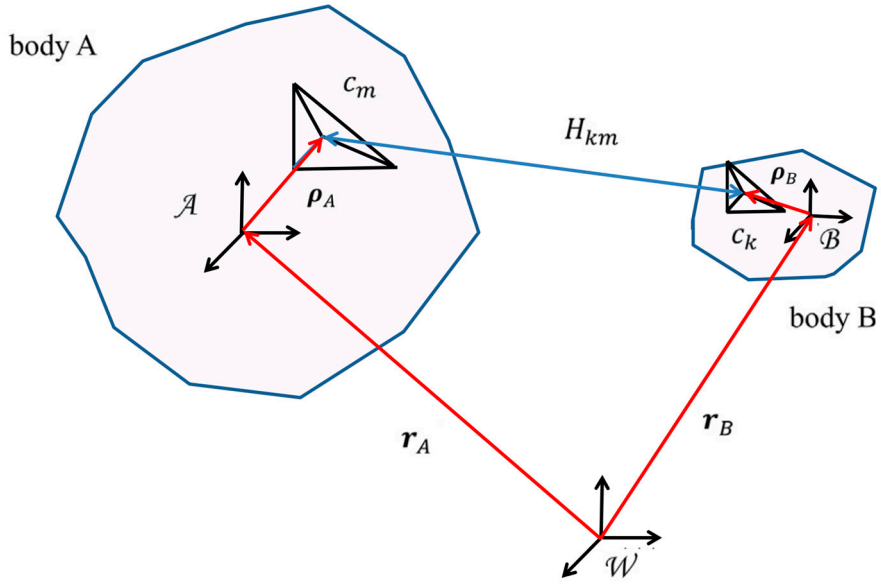

Figure 1. A geometric specification of the system.

In our model, tetrahedron c_k is from object A, and tetrahedron c_m is from object B. Bilinear interpolation is used on the integration fields of c_m and c_k [10]. Let $\boldsymbol{\rho}_A = (x_a, y_a, z_a)$ represent the arbitrary vertex position of element c_k, and let $\boldsymbol{\rho}_B = (x_b, y_b, z_b)$ represent the arbitrary vertex position of element c_m with $\boldsymbol{\rho}_A$ and $\boldsymbol{\rho}_B$ computed by A and B, respectively. The volume-based field integral of the interaction function h ($\boldsymbol{\rho}_A$, $\boldsymbol{\rho}_B$) over c_k and c_m is determined by the following equation:

$$H_{km} = \iiint_{c_m} \iiint_{c_k} h(\boldsymbol{\rho_A}, \boldsymbol{\rho_B}) \mathrm{d}x_a \mathrm{d}y_a \mathrm{d}z_a \mathrm{d}x_b \mathrm{d}y_b \mathrm{d}z_b \tag{1}$$

Next, we implemented natural coordinates and used bilinear interpolation to evaluate the function h ($\boldsymbol{\rho}_A$, $\boldsymbol{\rho}_B$) across the region occupied by the paired elements $\{c_k, c_m\}$. This allows for the precise analytical integration of Equation (1) within the defined domain:

$$H_{km} \approx \frac{1}{576} J_k^{-1} J_m^{-1} \sum_i \sum_j H_{ij}^{km} \tag{2}$$

J_k and J_m are the Jacobian determinants and H_{ij}^{km} are the shape functions of the tetrahedra, where, k and m are the indices of the elements in objects A and B, respectively, and i and j are the numbers of vertices of the two tetrahedra under consideration.

Let $\mathbb{A}$ and $\mathbb{B}$ be the sets of all elements within rigid bodies A and B, respectively. Then, the integral of the interaction function $h\left(\boldsymbol{\rho}_A, \boldsymbol{\rho}_B\right)$ over the entire two-body domain can be expressed as:

$$H = \sum_{k \in \mathbb{A}} \sum_{m \in \mathbb{B}} H_{km} \tag{3}$$

Because each node can simultaneously belong to multiple different elements, there are many redundant calculations in Equation (3). The sum in Equation (3) can be simplified by considering the mesh nodes of the two objects as follows:

$$H = \sum_{k \in \mathbb{A}} \sum_{m \in \mathbb{B}} H_{km} \approx \sum_{\alpha} \sum_{\beta} w_\alpha w_\beta H_{\alpha\beta} \tag{4}$$

α and β are the node indices of the integrand, $H_{\alpha\beta}$ represents the value of the interaction function at nodes α and β, and w_α and w_β are custom-defined node weights that are computed as follows:

$$w_\alpha = \frac{1}{24} \sum_{k \in \mathbb{C}_\alpha} J_k^{-1}, w_\beta = \frac{1}{24} \sum_{m \in \mathbb{D}_\beta} J_m^{-1} \tag{5}$$

$\mathbb{C}_\alpha$ is the set of all elements in object A containing the grid node α and $\mathbb{D}_\beta$ is the set of all elements in object B containing the node β.

The most time-consuming part of the analysis involves the calculation of the gravitational potential [18,19] during the integration process and the computation of both the gravitational forces on object A and the torques on objects A and B. As the scale of the mesh increases, the computational workload increases significantly.

For any arbitrary grid node α in object A and any arbitrary grid node β in object B, the gravitational force $\boldsymbol{f}_{\alpha\beta}$ acting on α by β and the torque $\boldsymbol{p}_{\alpha\beta}$ acting on the center of mass of object A can be derived from the gravitational force exerted by β on α, and the torque $\boldsymbol{q}_{\alpha\beta}$ acting on the center of mass of object B can be derived from the gravitational force exerted by α on β, with G being the constant of universal gravitation. The function $\sigma_A(\rho_{A\alpha})$ describes the density distribution inside body A and $\sigma_B(\rho_{B\beta})$ describes that inside body B:

$$\boldsymbol{f}_{\alpha\beta} = \mathrm{G}\boldsymbol{\sigma}(\boldsymbol{\rho}_{A\alpha})\boldsymbol{\sigma}(\boldsymbol{\rho}_{B\beta}) \frac{\boldsymbol{r}_{A\alpha} - \boldsymbol{r}_{B\beta}}{\left|\boldsymbol{r}_{A\alpha} - \boldsymbol{r}_{B\beta}\right|^3} \tag{6}$$

$$\boldsymbol{p}_{\alpha\beta} = \mathrm{G}\boldsymbol{\sigma}(\boldsymbol{\rho}_{A\alpha})\boldsymbol{\sigma}(\boldsymbol{\rho}_{B\beta}) \frac{\boldsymbol{\rho}_{A\alpha} \times (\boldsymbol{r}_{A\alpha} - \boldsymbol{r}_{B\beta})}{\left|\boldsymbol{r}_{A\alpha} - \boldsymbol{r}_{B\beta}\right|^3} \tag{7}$$

$$\boldsymbol{q}_{\alpha\beta} = \mathrm{G}\boldsymbol{\sigma}(\boldsymbol{\rho}_{A\alpha})\boldsymbol{\sigma}(\boldsymbol{\rho}_{B\beta}) \frac{\boldsymbol{\rho}_{B\beta} \times (\boldsymbol{r}_{A\alpha} - \boldsymbol{r}_{B\beta})}{\left|\boldsymbol{r}_{A\alpha} - \boldsymbol{r}_{B\beta}\right|^3} \tag{8}$$

According to Equation (4), we can estimate the gravitational forces on objects A and B as well as the torques on both objects by using bilinear tetrahedra:

$$\boldsymbol{F}_{AB} = \sum_{\alpha} \sum_{\beta} w_\alpha w_\beta \boldsymbol{f}_{\alpha\beta} \tag{9}$$

$$\boldsymbol{T}_A = \sum_{\alpha} \sum_{\beta} w_\alpha w_\beta \boldsymbol{p}_{\alpha\beta} \tag{10}$$

$$\boldsymbol{T}_B = \sum_{\alpha} \sum_{\beta} w_\alpha w_\beta \boldsymbol{q}_{\alpha\beta} \tag{11}$$

For the sake of convenience in derivation, the following definitions for W_α and W_β are introduced:

$$W_\alpha = w_\alpha \sigma(\boldsymbol{\rho}_{A\alpha}) \tag{12}$$

$$W_\beta = w_\beta \sigma(\boldsymbol{\rho}_{B\beta}) \tag{13}$$

Therefore, Equations (9)–(11) can be rewritten as:

$$\boldsymbol{F}_{AB} = \mathrm{G}\sum_{\alpha}\sum_{\beta} W_\alpha W_\beta \frac{\boldsymbol{r}_{A\alpha} - \boldsymbol{r}_{B\beta}}{\left|\boldsymbol{r}_{A\alpha} - \boldsymbol{r}_{B\beta}\right|^3} \tag{14}$$

$$\boldsymbol{T}_A = \mathrm{G}\sum_{\alpha}\sum_{\beta} W_\alpha W_\beta \frac{\boldsymbol{\rho}_{A\alpha} \times (\boldsymbol{r}_{A\alpha} - \boldsymbol{r}_{B\beta})}{\left|\boldsymbol{r}_{A\alpha} - \boldsymbol{r}_{B\beta}\right|^3} \tag{15}$$

$$\boldsymbol{T}_B = \mathrm{G}\sum_{\alpha}\sum_{\beta} W_\alpha W_\beta \frac{\boldsymbol{\rho}_{B\beta} \times (\boldsymbol{r}_{A\alpha} - \boldsymbol{r}_{B\beta})}{\left|\boldsymbol{r}_{A\alpha} - \boldsymbol{r}_{B\beta}\right|^3} \tag{16}$$

2.2. Calculation of Binary Asteroid Interaction Forces

The computation processes for the gravitational potential, gravitational force on A, torque on A, and torque on B are as follows.

(1) Input double precision data $\boldsymbol{r}_{Ai}$, $\boldsymbol{r}_{Bj}$, $\boldsymbol{\rho}_{Ai}$, $\boldsymbol{\rho}_{Bj}$, $\boldsymbol{W}_{Ai}$, and $\boldsymbol{W}_{Bj}$, where $\boldsymbol{W}_{Ai}$ is the product of $\mathbf{w}_{Ai}$ and $\sigma(\boldsymbol{\rho}_{Ai})$ and $\boldsymbol{W}_{Bj}$ are the product of $\mathbf{w}_{Bj}$ and $\sigma(\boldsymbol{\rho}_{Bj})$.
(2) Compute Equations (14)–(16).
(3) Output the results $\boldsymbol{F}_{\mathrm{AB}}$, $\boldsymbol{T}_{\mathrm{A}}$, and $\boldsymbol{T}_{\mathrm{B}}$.

In the computation process on a single-core CPU, the procedure is as follows. First, the parameters associated with the nodes in objects A and B are iteratively read. These parameters are then used to compute $\boldsymbol{f}_{ij}$, $\boldsymbol{p}_{ij}$, and $\boldsymbol{q}_{ij}$ for each iteration, where:

$$\boldsymbol{f}_{ij} = W_{Ai} W_{Bj} \frac{\boldsymbol{r}_{Ai} - \boldsymbol{r}_{Bi}}{\left|\boldsymbol{r}_{Aj} - \boldsymbol{r}_{Bj}\right|^3} \tag{17}$$

$$\boldsymbol{p}_{ij} = \boldsymbol{\rho}_{Ai} \times \boldsymbol{f}_{ij} \tag{18}$$

$$\boldsymbol{q}_{ij} = \boldsymbol{\rho}_{Bj} \times \boldsymbol{f}_{ij} \tag{19}$$

Then, all the computed $\boldsymbol{f}_{ij}$, $\boldsymbol{p}_{ij}$, and $\boldsymbol{q}_{ij}$ values are summed and multiplied by G to obtain $\boldsymbol{F}_{AB}$, $\boldsymbol{T}_A$, and $\boldsymbol{T}_B$, respectively. Notably, the rigid body A has N_1 nodes, and the rigid body B has N_2 nodes, and it requires $N_1 \times N_2$ iterations to obtain $N_1 \times N_2$, $\boldsymbol{f}_{ij}$, $\boldsymbol{p}_{ij}$, and $\boldsymbol{q}_{ij}$ values.

The most time-consuming part of the program is the computation of the gravitational force and torque between the binary asteroids, i.e., $\boldsymbol{F}_{AB}$, $\boldsymbol{T}_A$, and $\boldsymbol{T}_B$. The W_α and W_β terms in Equations (12) and (13) are constants, and they only need to be computed once during preprocessing for each node. For the computation of $\boldsymbol{f}_{ij}$, the $\boldsymbol{r}_{Ai}$ term, which is the sum of the mass position vectors of object A, needs to be computed. The computation method for $\boldsymbol{\rho}_{Ai}$ and $\boldsymbol{r}_{Bj}$ is similar. This step involves two addition operations of the 3D vectors. Subsequently, Equation (17) is computed, which involves one subtraction operation of the 3D vectors, one modulus operation of the 3D vectors, four double precision floating point multiplications, and one scaling operation of the 3D vectors. For the computation of $\boldsymbol{p}_{ij}$, only the cross product of $\boldsymbol{\rho}_{Ai}$ and $\boldsymbol{f}_{ij}$ (Equation (18)) needs to be computed. This process includes one cross product operation of the 3D vectors, and the computation of $\boldsymbol{q}_{ij}$ is similar. In general, for each computation of the interaction between two objects, the summation process involves $3 \times (N_1 \times N_2 - 1)$ addition operations of the 3D vectors.

The use of CUDA (Compute Unified Device Architecture) for acceleration enables the replacement of loops with parallel functions. As the binary system evolves, the positions and orientations of the two bodies change over time, which affects the values of $\boldsymbol{F}_{AB}$, $\boldsymbol{T}_A$, and $\boldsymbol{T}_B$. However, because mesh partitioning only needs to be executed once during the program's runtime, its computational cost is negligible. The most time-consuming aspect

is the computation of $\boldsymbol{F}_{AB}$, $\boldsymbol{T}_A$, and $\boldsymbol{T}_B$ in each integration step. As the computations for each node pair (i, j) occur simultaneously at each time step, this step is best suited for parallelization. The computation of $\boldsymbol{f}_{ij}$ for each node pair (i, j) is independent of the others, and the same applies to $\boldsymbol{p}_{ij}$ and $\boldsymbol{q}_{ij}$, which makes this a typical parallel computation. Therefore, the computation of $\boldsymbol{F}_{AB}$, $\boldsymbol{T}_A$, and $\boldsymbol{T}_B$ at each time step is parallelized, whereas other tasks, such as mesh partitioning, integration, and post-processing, are still handled by the CPU.

The parallel algorithm employs two kernel functions. One calculates the interaction forces and torques between every pair of nodes, and the other simplifies these calculations. The first kernel function starts from a two-dimensional grid of size (N_1, N_2) (assuming that object A has N_1 nodes and object B has N_2 nodes). Each thread in the 2D grid computes $\boldsymbol{f}_{ij}$, $\boldsymbol{p}_{ij}$, and $\boldsymbol{q}_{ij}$ for nodes related to the x-coordinate i in object A and the y-coordinate j in object B by using Equations (17)–(19). Each thread processes information, such as the position and density of the ith node in object A and jth node in object B. The function then outputs the resulting vectors of forces and torques contributed by each node from both objects.

After computing the two-dimensional grid, the $\boldsymbol{f}_{ij}$, $\boldsymbol{p}_{ij}$, and $\boldsymbol{q}_{ij}$ values between each pair of element nodes in objects A and B are obtained. The quantity of each parameter is $N_1 \times N_2$, and these parameters are summed to obtain $\boldsymbol{F}_{AB}$, $\boldsymbol{T}_A$, and $\boldsymbol{T}_B$. In the second kernel function, we employed a binary tree approach to streamline the data. By simplifying the data on the GPU before transferring them to the host computer, we can reduce bandwidth demands and enhance the efficiency of data transmission [20].

To better understand and calculate the routines related to the forces and moments of a binary asteroid system, we edited the algorithms in Sections 2.1 and 2.2 into Algorithms 1 and 2, respectively, and attached flowcharts, as shown in Figure 2. In order to facilitate the readers' understanding of the operational relationships of these variables, we added the following figure for clarification.

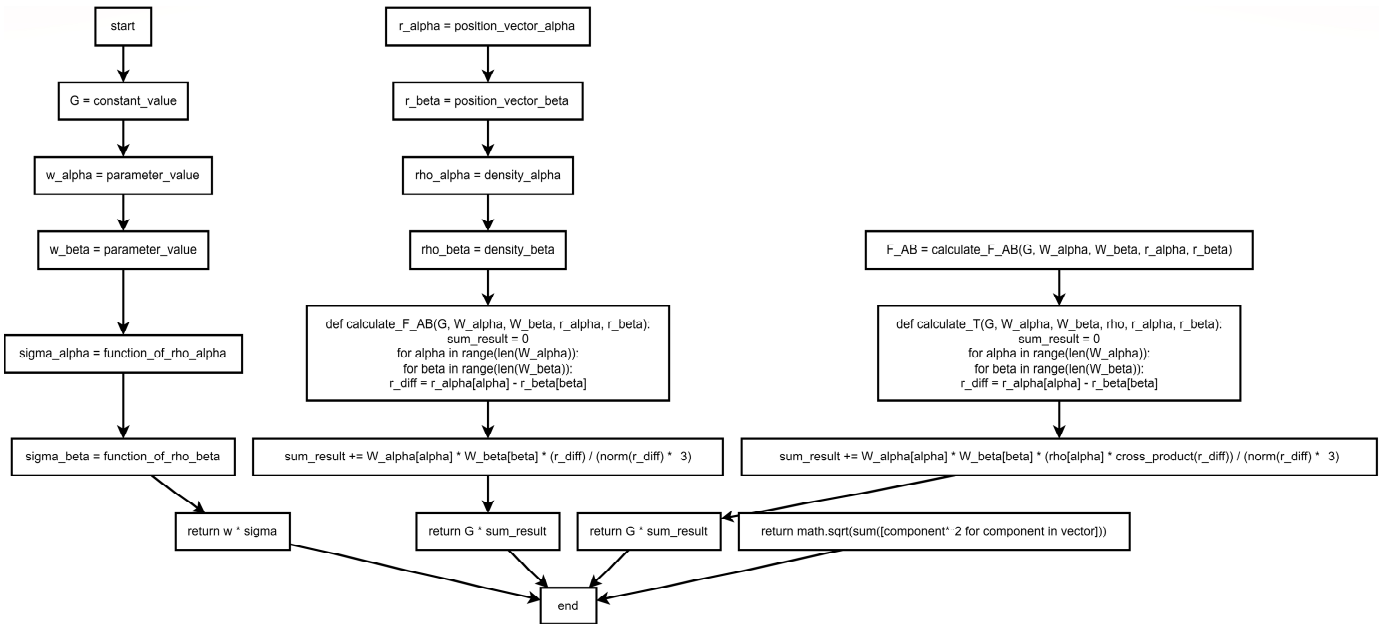

Figure 2. The pseudo-code and flow diagrams for Sections 2.1 and 2.2.

Algorithm 1 Calculation of Forces and Torques in a Physical System.

 # Constants and Parameters
$G \leftarrow$ constant_valne ▷Gravitational constant or another defined constant
$\omega_\alpha \leftarrow$ parameter_value ▷Parameter ω for α
$\omega_\beta \leftarrow$ parameter_value ▷Parameter ω for β
$\sigma_\alpha \leftarrow$ function_of_rho_alpha ▷Function of density for α
$\sigma_\beta \leftarrow$ function_of_rho_beta ▷Function of density for β
function CALCULATE_W(ω, σ)
    return $\omega \times \sigma$
end function
$W_\alpha \leftarrow$ calculate_W(ω_α, σ_α)
$W_\beta \leftarrow$ calculate_W(ω_β, σ_β)
 # Position vectors r **and density** ρ
$r_\alpha \leftarrow$ position_vector_alpha ▷Position vector for α
$r_\beta \leftarrow$ position_vector_beta ▷Position vector for β
$\rho_\alpha \leftarrow$ density_alpha ▷Density for α
$\rho_\beta \leftarrow$ density_beta ▷Density for β
function CALCULATE_F_AB (G, W_α, W_β, r_α, r_β)
    sum_result $\leftarrow 0$
    for α **in** range(len(W_α)) **do**
        for β **in** range(len(W_β)) **do**
            r_diff $\leftarrow r_\alpha[\alpha] - r_\beta[\beta]$
            sum_result $\leftarrow$ *sum_result* + $W_\alpha[\alpha] \times W_\beta[\beta] \times$ *r_diff* /(norm(*r_diff*)^3)
        end for
    end for
    return $G \times$ *sum_result*
end function
F_AB $\leftarrow$ calculate_F_AB (G, W_α, W_β, r_α, r_β)
function CALCULATE_T (G, W_α, W_β, ρ, r_α, r_β)
    sum_result $\leftarrow$0
    for α **in** range(len(W_α)) **do**
        for β **in** range(len(W_β)) **do**
        r_diff $\leftarrow r_\alpha[\alpha] - r_\beta[\beta]$
            sum_result $\leftarrow$ *sum_result* + $W_\alpha[\alpha] \times W_\beta[\beta] \times (\rho[\alpha] \times$ cross_product(*r_diff*))/(norm(*r_diff*)^3)
        end for
    end for
    return $G \times$ *sum_result*
end function
$T_A \leftarrow$ calculate_T (G, W_α, W_β, ρ_α, r_α, r_β)
$T_B \leftarrow$ calculate_T (G, W_α, W_β, ρ_β, r_α, r_β)
 # Auxiliary Functions
function NORM (*vector*)
    return $\sqrt{\sum_{\text{component}} \text{component}^2}$
end function
function CROSS_PRODUCT (*vector*)
    return [*vector* [1] $\times$ *vector* [2], *vector* [2] $\times$ *vector* [0], *vector* [0] $\times$ *vector* [1]]
end function

Algorithm 2 Calculation of Interaction Terms in a Physical System.

function CALCULATE_F_IJ (W_α, W_β, r_α, r_β)
  f_{ij}←[]
  for $i \in$ range(len(W_α)) **do**
    for $j \in$ range(len(W_β)) **do**
      $r_diff \leftarrow r_\alpha[i] - r_\beta[j]$
      $f_{ij_value} \leftarrow W_\alpha[i] \times W_\beta[j] \times r_diff/(\text{norm}(r_diff)^3)$
      append f_{ij_value} to f_{ij}
    end for
  end for
  return f_{ij}
end function
function CALCULATE_P _IJ (ρ_α, f_{ij})
  p_{ij}←[]
  for $i \in$ range(len(ρ_α)) **do**
    for $j \in$ range(len(f_{ij})) **do**
      $p_{ij_value} \leftarrow \rho_\alpha[i] \times f_{ij}[j]$
      append p_{ij_value} to p_{ij}
    end for
  end for
  return p_{ij}
end function
function CALCULATE_Q _IJ (ρ_β, f_{ij})
  q_{ij}←[]
  for $i \in$ range(len(ρ_β)) **do**
    for $j \in$ range(len(f_{ij})) **do**
      $q_{ij_value} \leftarrow \rho_\beta[i] \times f_{ij}[j]$
      append q_{ij_value} to q_{ij}
    end for
  end for
  return q_{ij}
end function
$f_{ij} \leftarrow$ calculate_f_ij (W_α, W_β, r_α, r_β)
$p_{ij} \leftarrow$ calculate_p _ij (ρ_α, f_{ij})
$q_{ij} \leftarrow$ calculate_q _ij (ρ_β, f_{ij})
function NORM (*vector*)
  return $\sqrt{\sum_{\text{component} \in \text{vector}} \text{component}^2}$
end function

2.3. Double Asteroid Motion–Attitude Simulation

Based on the discussion in the previous section, to balance the accuracy and efficiency of our GPU parallel program, we applied CUDA-C parallel programming to model the binary asteroid (66391) 1999 KW4. The physical properties of this asteroid are outlined in Table 1, and its shapes are illustrated in Figure 3. This simulation describes the motion of the binary asteroid 1999 KW4, where KW4 A is the larger primary asteroid and KW4 B is the smaller secondary asteroid. The simulation focuses on the interactions driven by mutual gravitational forces.

Table 1. Iterative calculation requirements for each value.

Variable	Computed Once	Computed on Each Iteration	Notes
W_α, W_β	Yes	No	Constants from Equations (12) and (13), precomputed per node.
W_{Ai}, W_{Bj}	Yes	No	Products of w_{Ai}, w_{Bj} and constants W_α, W_β.
ρ_{Ai}, ρ_{Bj}	Yes	No	Node densities, assumed constant if asteroids do not deform.
r_{Ai}, r_{Bj}	No	Yes	Node positions, changing over time as asteroids move.
f_{ij}	No	Yes	Depends on current node positions r_{Ai}, r_{Bj}.
p_{ij}, q_{ij}	No	Yes	Depend on f_{ij} and possibly node orientations.
F_{AB}, T_A, T_B	No	Yes	Sums over f_{ij}, p_{ij}, $q_{ij}$are updated at each time step.

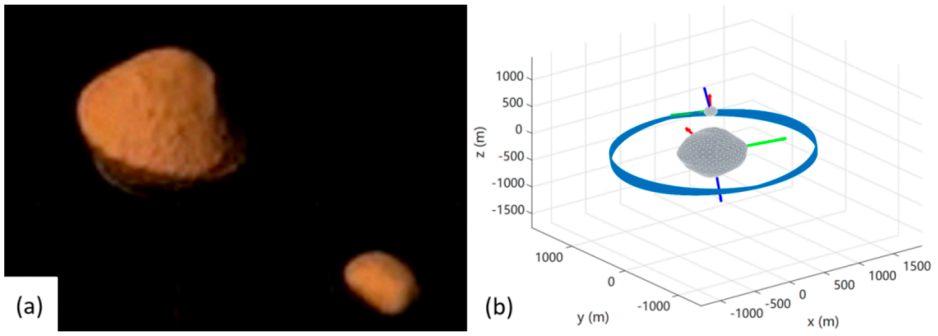

Figure 3. Binary system of 1999 KW4: (**a**) image of the binary asteroid system 1999 KW4 captured by NASA; (**b**) simulated trajectory of the 1999 KW4 system.

To clarify the operation of the parallel procedure, it is important to note that not all tasks are performed on the GPU. Only the computations of $\boldsymbol{F}_{AB}$, $\boldsymbol{T}_A$, and $\boldsymbol{T}_B$, which are the most time-consuming and suitable for parallel processing during each integration step, are assigned to the GPU [21]. Other tasks, such as data initialization and integration, remain the responsibilities of the CPU. The positions of KW4 A and KW4 B were defined in an inertial system centered at the center of mass of the asteroid system. Assuming that KW4 B is in the locked phase, its initial velocity was set to match a circular orbit. An adaptive step-size Runge–Kutta–Fehlberg integrator was employed to simulate the dynamics of a binary asteroid across ten orbital cycles. The core code was executed with the final results and system parameters listed in Table 2.

Table 2. Physical properties of the 1999 KW4 binary asteroid system.

Physical Property	Value
Double asteroid orbital week T_{orb}	17.4 h
Orbital diameter of companion asteroid	2.54 km
Ratio of the companion's diameter to that of the primary asteroid	0.34

To simulate and analyze the spacecraft orbits within the dual asteroid system, we set up an experimental environment utilizing high-performance computing resources. Specifically, we employed an NVIDIA GTX1060 graphics processor (Santa Clara, CA, USA) with the following specifications: Graphics Processor: GTX1060, Memory Frequency: 8.008 GHz,

GPU Memory Size: 6 GB, and CUDA Cores: 1280. These hardware configurations enabled the efficient processing of the finite element simulations and real-time orbital computations necessary for our study.

3. Generation of Probe Orbits

3.1. Types of Probe Orbits

Although observations from multiple angles and positions are possible for flyby missions targeting binary asteroid systems, the brief duration of these flyby missions presents challenges in collecting extensive information about the system [22,23]. Therefore, analyzing the orbits of missions around binary asteroids is considered to be the best approach for their exploration [24]. Two types of orbits are primarily used for binary asteroid systems: horizontal orbit usually refers to an orbit that is parallel or nearly parallel to the reference plane (such as the equatorial plane of the asteroid host star), which offers a better coverage of the equatorial regions of the primary and companion bodies; vertical orbit usually refers to an orbit where the orbital plane is perpendicular or nearly perpendicular to the reference plane (such as the equatorial plane of the asteroid's main star), which is better suited for studying the polar regions of the primary body. Combining these two types of orbits allows for a thorough exploration [25,26] of a binary asteroid system. This section focuses on analyzing these two distinct orbits, which are adaptable and satisfy various mission requirements.

3.2. Simulating the Orbit of the Probe

All position and direction vectors in the text are defined in an inertial reference frame. This is a fixed reference frame that facilitates the description of the absolute motion state of an object. In this case, for the convenience of displaying the motion results of the detector and binary system, an inertial reference frame is established at the center of the main star, and the initial position of the companion star is defined as the positive direction of its *X*-axis. Building on the previous method, after acquiring the position and velocity data for the binary asteroid system 1999 KW4 by using the finite element method, we can use these data to determine the positions of irregular, time-varying binary asteroids. Adding a probe to this scenario allowed us to establish a restricted three-body problem involving binary asteroids and a probe. Given that the mass and volume of the probe are considerably smaller than those of the binary asteroids, its representation can be simplified to a point mass. And the motion of the probe is always within the gravitational Hill sphere of the binary star. This adjustment simplifies the scenario to a restricted three-body problem. Various orbital patterns can be explored by assigning different initial positions and velocities to the probe. Figure 4 shows four typical simulation results for the vertical orbits around the binary asteroid system.

The initial attitude data of the asteroid is presented in Table 3, and the initial conditions of the detector on each orbit are shown in the following table.

As shown in the Figure 4, the main difference among the four orbit types is the initial entry position of the probe. In groups A–D, the initial entry positions progressively move closer to the primary body within the binary asteroid system. By observing the evolution of these orbits, it is clear that different entry positions have a significant impact on the trajectory of the probe. Although some orbits initially followed the expected patterns, notable variations were observed in their subsequent development.

By analyzing the horizontal circumnavigation orbits, we can explore the equatorial regions of both the primary and companion bodies within the binary asteroid system. Similarly, by adjusting the velocity vector at the point of orbit entry, the vertical circumnavigational orbits can be examined. For a straightforward comparison, by controlling the initial positions of the two asteroids to remain unchanged and the initial position of the detector to always be on the x = y line in the third quadrant, four sets of typical orbits were analyzed from the same entry position, as shown in Figure 5.

Table 3. The initial conditions of the detector for each orbit.

Orbit	Coordinate X/m	Coordinate Y/m	Coordinate Z/m	Vx/ (cm/s)	Vy/ (cm/s)	Vz/ (cm/s)
A	−3000	−3000	50	1	1	10
B	−2500	−2500	50	1.5	1.5	11.5
C	−2000	−2000	50	2	2	12
D	−1500	−1500	50	3.5	3.5	16.5
E	−3000	−3000	50	7	−7	1
F	−2500	−2500	50	8	−8	1.5
G	−2000	−2000	50	10	−10	2
H	−1500	−1500	50	12.5	−12.5	3

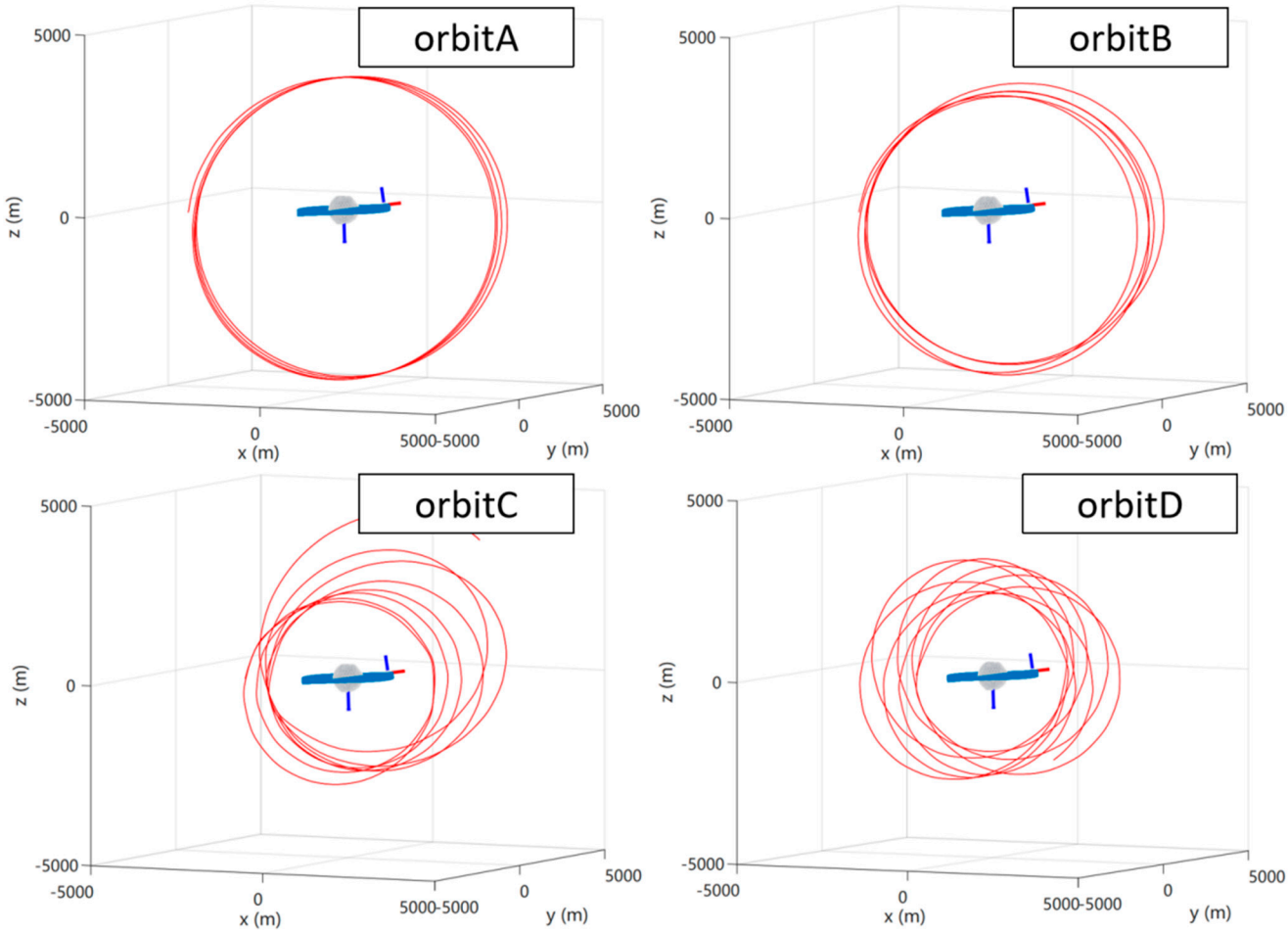

Figure 4. Simulation results for the vertical circular orbits of the ABCD group of the binary asteroid system.

In these four orbit types, the key difference is the varying entry position of the probe. From groups E to H, the initial entry positions progressively approached the primary body within the binary asteroid system. Observations of the evolution of these orbits showed that, similar to the observations of the vertical circumnavigation group, the impact of different entry positions on the trajectory of the probe is substantial. Although some orbits initially followed the expected patterns, significant differences were observed as they developed. However, some characteristics of these orbital evolutions differed from those that were observed in the vertical circumnavigation group.

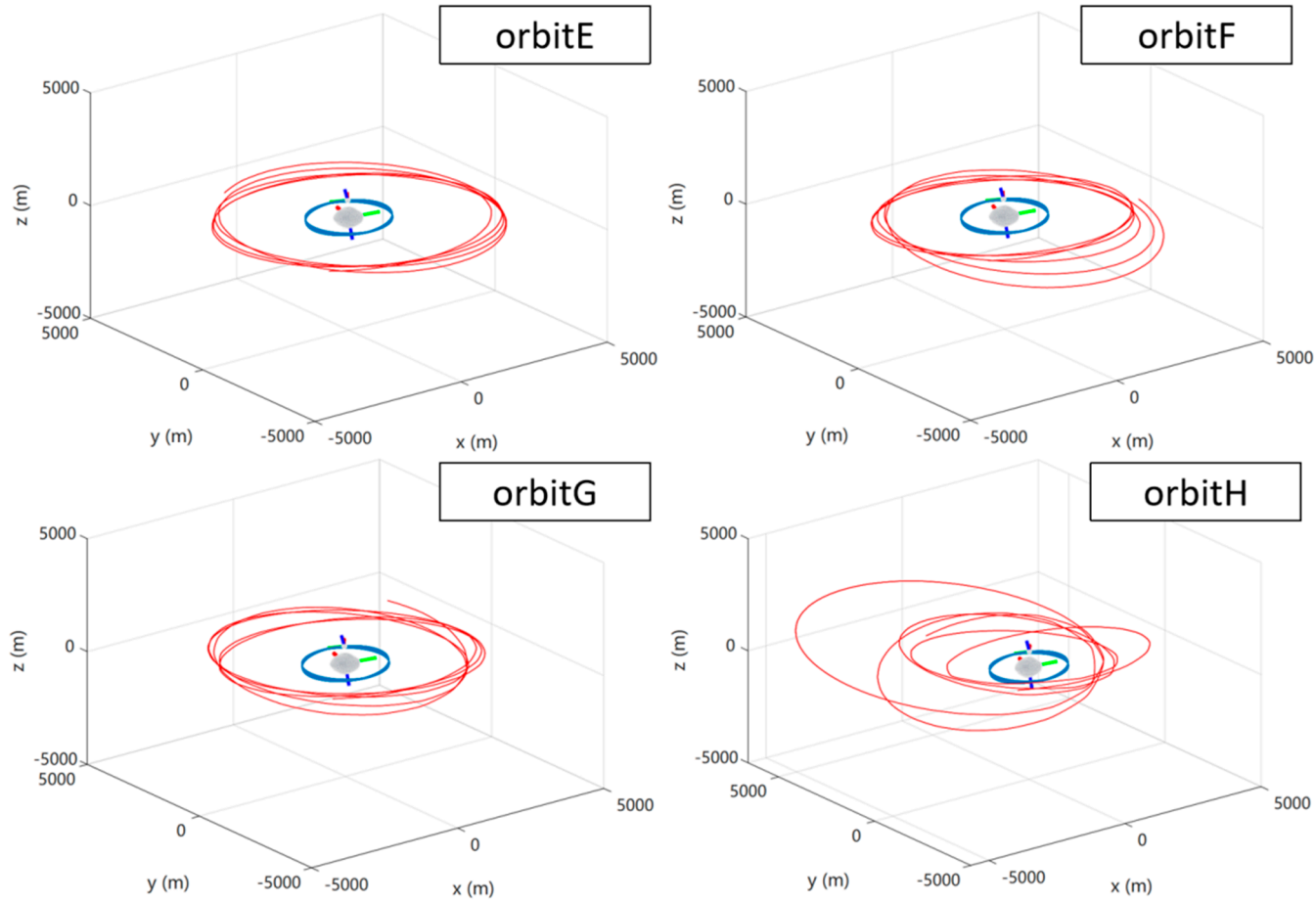

Figure 5. Simulation results for the horizontal circumnavigation orbits of the EFGH group within the binary asteroid system.

4. Orbital Analysis of Double Asteroid System Probe

4.1. Contrasting Probe Orbits of Different Models

The accuracy of the time-varying binary asteroid system modeled using the finite element model can by demonstrated by comparing the orbit of the probe to that generated by using the older double ellipsoid modeling approach. By comparing the orbital evolution of the probe under identical initial velocity and positional conditions in these two models, the superiority of the finite element model becomes clear. For simplicity, we focused only on the variations in the velocity and position of the detector along the x-axis. This targeted comparison effectively illustrates the improvements, as shown in Figure 6, in which both models display a periodically increasing and decreasing velocity pattern. However, significant differences were observed in these parameters. The finite element model, which accounts for the time-varying and irregular characteristics of binary asteroids, shows the impact on the detector velocity, particularly through minor fluctuations at peak values. This also led to a significant deviation in subsequent displacement to some extent. These observations highlight the superior ability of the finite element model to simulate gravitational field variations within a binary asteroid system.

The differences in velocity between the two models led to discrepancies in the positional changes in the detector. Although both models exhibited periodic shifts in position, the double ellipsoid model, which did not account for the irregular and time-varying characteristics of the binary asteroid system, exhibited slower positional changes. Consequently, it took noticeably longer for the detector to reach the same position in the ellipsoid model than in the finite element model.

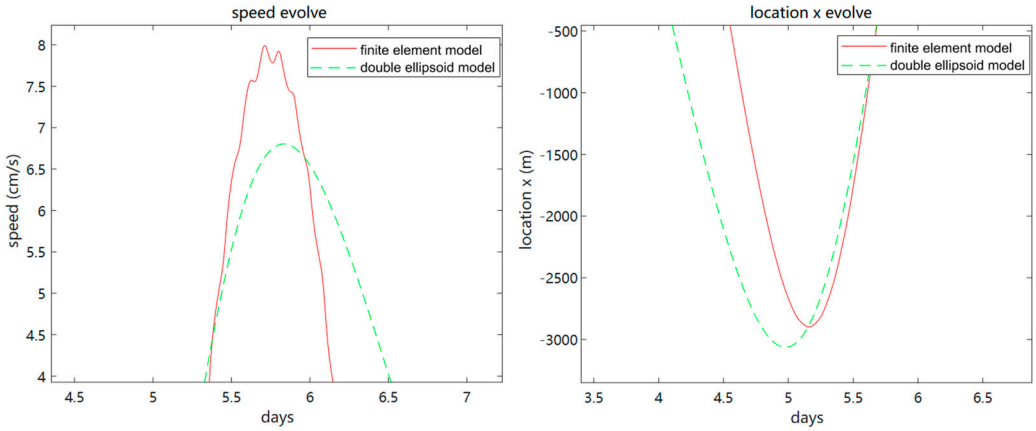

Figure 6. Probe velocity variations and the variations in the detector positions for two models of binary asteroid systems.

4.2. Analysis of Orbital Characteristics of Double Asteroid System Probe

To characterize the orbital features, the number of orbital hexagons typically indicates the detector's orbital position [27–29]. Instead of focusing on the position of the detector, analyzing its orbital characteristics and velocity can provide valuable insights. By considering the sum of the vector velocities rather than the true perigee angle, we can focus on the velocity characteristics of the detector. Comparing the eccentricities, orbital inclinations, ascending node declinations, perigee angles, and velocity values allows for a preliminary assessment of the stability of different detector orbits. Owing to variations in the orbital periods among different orbit types, this study used the mutual orbital period of the binary asteroid system as the standard time axis for the analysis. Plotting the semi-major axes of the detector orbits for the ABCD and EFGH groups along with the changes in eccentricity offers a clear view of the orbital parameters, as shown in Figure 7.

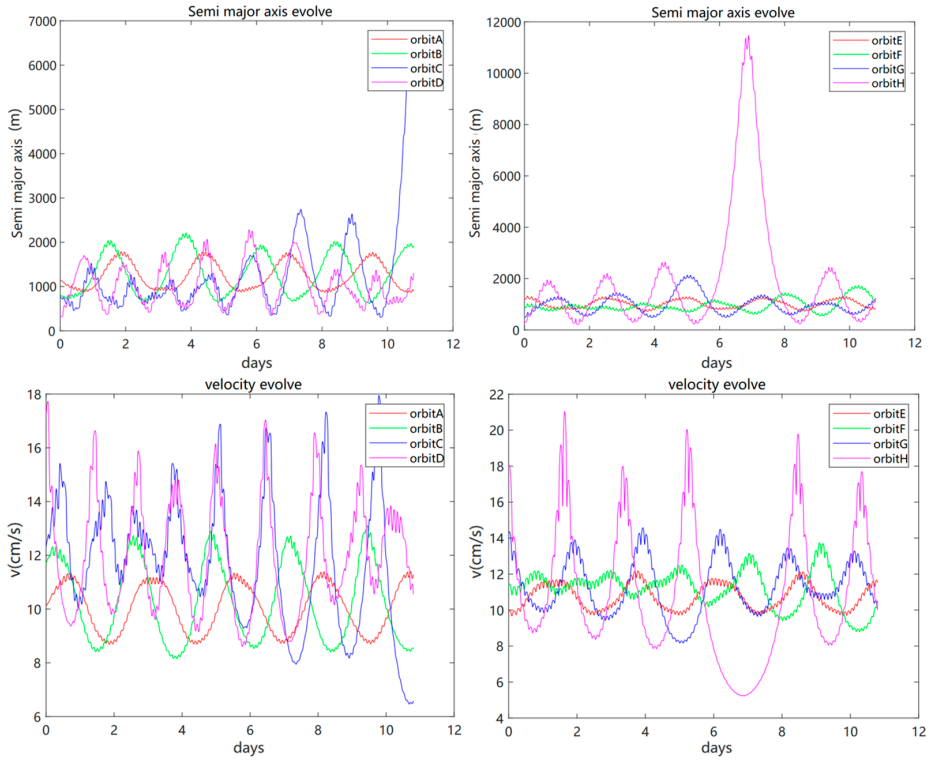

Figure 7. Variation in the semi-major axes and detector velocities of the binary asteroid system orbital paths.

In the orbit analysis, the semi-major axis largely sets the altitude of the detector's orbit, whereas the detector's velocity influences the time required to reach various positions. These two parameters significantly affected the overall quality of the detector survey. However, when planning orbits for binary systems, there is a risk of collision if the orbital altitude of the detector is lower than that of the companion asteroid. This scenario is undesirable for orbit analysis. To ensure the safety of the detector and avoid collisions, the semi-major axis of the companion asteroid was subtracted during statistical plotting. By comparing the changes in the semi-major axis and detector velocity between the ABCD and EFGH groups, orbits within a distance of 500–1000 m from the binary β-asteroid companion were identified. Specifically, orbits CD and GH initially maintain stability, but significantly diverge after to 4–6 cycles of the binary asteroid, compared to orbits AB and EF, which were 1000–1500 m away from the companion's orbit. In addition, the divergence in velocities varied between the horizontal and vertical orbit groups. The velocity range for the vertical orbit ABCD group is 6–18 cm/s, whereas the horizontal orbit EFGH group spans 4–22 cm/s under the same initial conditions.

By analyzing the range of variations in the orbital semi-major axis, we drew similar conclusions. For orbits within a range of 500–1000 m from the orbit of the binary asteroid companion, such as the CD and GH groups, the divergence of the semi-major axis in the later stages is more pronounced. However, for orbits within the range of 1000–1500 m from the companion orbit, such as the AB and EF groups, although the semi-major axis also exhibits periodic variations, it still maintains stability in the numerical range after 10 cycles. This indicates that, for the binary asteroid system 1999 KW4, maintaining the orbit altitude of the detector at least 1000 m above the companion orbit can help preserve orbit stability without the need for fuel-intensive orbit corrections. Additionally, choosing a vertical orbit over a horizontal orbit can lead to more stability in the detector's orbit semi-major axis and velocity and can thereby reduce the frequency of orbit corrections. This difference is likely because of the orientation of the orbital planes. Compared to vertical orbits, detectors in horizontal orbits are more likely to have close encounters with companion asteroids. Although this proximity can be beneficial for detailed observations of the companion, it may also lead to orbital resonance and thereby affect the stability of the detector's orbit.

In an orbital analysis, the eccentricity of an orbit shapes its fundamental structure. In particular, it influences where the detector's closest and farthest points from the center (i.e., the pericenter and apocenter) lie. The orbital inclination describes the extent to which the detector's orbital plane tilts, compared to the reference plane of the binary asteroid, which affects both the trajectory of the detector and its observational coverage of the binary asteroid system. These factors make both parameters crucial for comprehensive orbital analyses and operations. By determining the eccentricity and orbital inclination of the detector orbits for the ABCD and EFGH groups, we were able to visualize and understand these variations, as illustrated in Figure 8.

By comparing the changes in eccentricity and orbital inclination between the ABCD and EFGH groups, it is clear that, in the vertical orbit group, group C shows the most significant variation in eccentricity. In the horizontal orbit groups, group H exhibited the greatest variation. This observation generally supports the trend that shorter semi-major axes are associated with lower stability. However, this does not fully explain why, in the vertical orbit group, group D had less variation in eccentricity than group C. Considering scenarios in the simulation in which the detector may have had close encounters with the companion asteroid that led to its potential ejection from the system owing to gravitational forces, it is possible that the detector in group C of the vertical orbit group experienced closer encounters with the companion asteroid. However, further research is required to elucidate the exact reasons for these observations.

In terms of orbital inclination variations, groups C and D within the vertical-orbiting group and group H within the horizontal orbit group exhibited significant changes in orbital inclination. This aligns with the general trend that orbits with smaller semi-major axes are less stable. Moreover, the deviations in both groups' inclinations are approximately

0.4 radians, which further corroborates this trend. However, notable differences were observed in the patterns of local inclination variations between the two groups. The inclinations of both groups exhibited local fluctuations, but the vertical orbit group showed significantly larger fluctuations than did the horizontal orbit group. Local fluctuations in the orbital inclination of the companion asteroid in the vertical orbit group were typically approximately 0.05 radians. In contrast, fluctuations in the horizontal orbit group were an order of magnitude smaller, indicating greater stability in the orbital inclination of the horizontal orbit group.

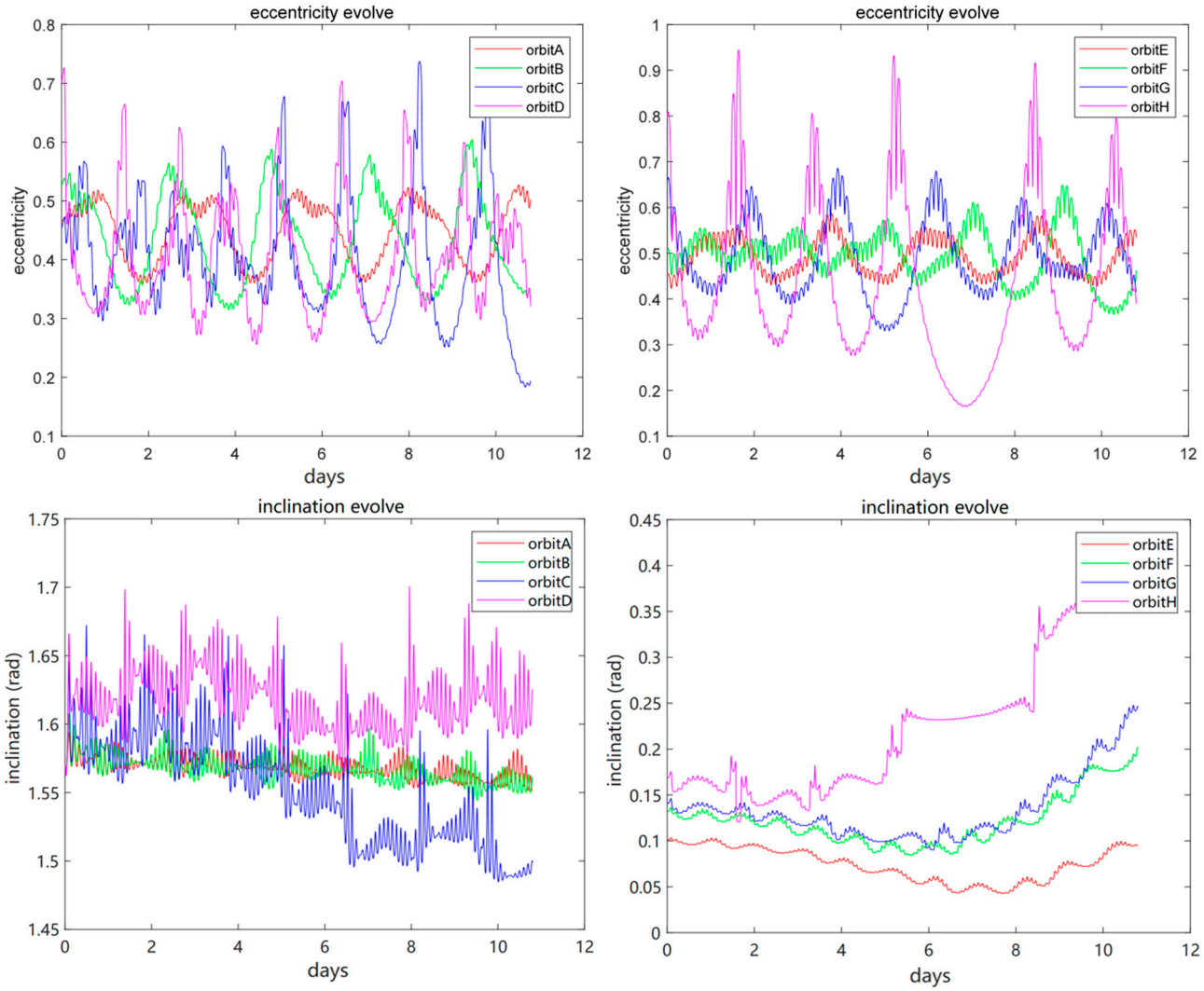

Figure 8. Variations in eccentricity and orbital inclination in the orbital analysis of the binary asteroid system.

In an orbital analysis, the right ascension of the ascending node is crucial because it determines the longitude at which the detector's orbit crosses the equatorial plane of binary asteroids. This intersection point indicates the detector's relative position in space and impact areas that can be observed during the mission, making it vital for planning purposes. However, the argument of the perigee is the angle between the line from the perigee to the ascending node and the line from the perigee to the focus of the elliptical orbit with Earth as its focus. This angle affects the shape of the detector's orbit and its operational state. Hence, it influences the velocity and altitude as the satellite moves along its orbit. Both parameters are crucial for a detailed orbital analysis and operation. By examining the changes in the right ascension of the ascending node and argument of the perigee for the

orbits in the ABCD and EFGH groups, we extracted valuable orbital parameter data, as illustrated in Figure 9.

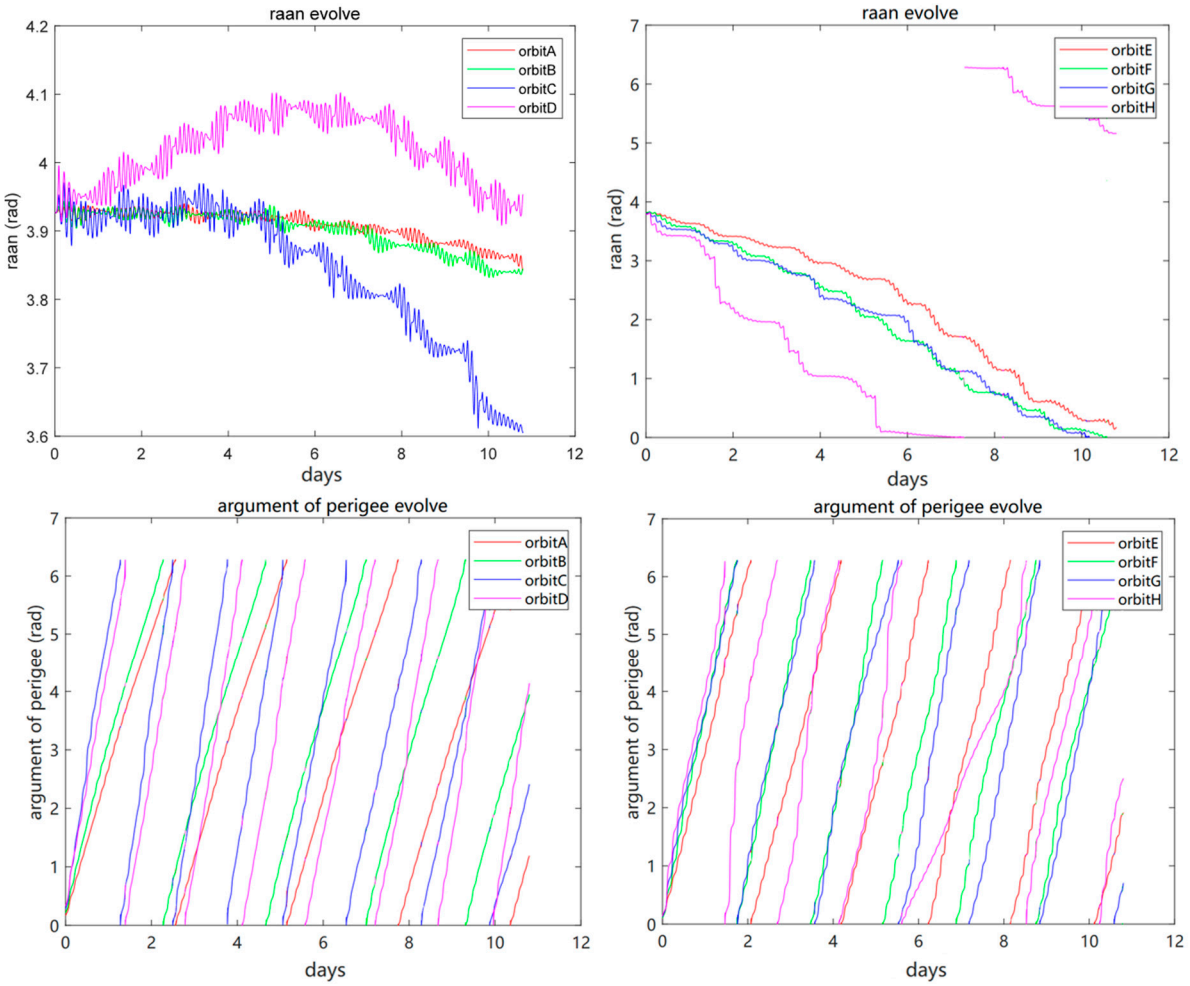

Figure 9. Variations in the right ascension of the ascending node and the argument of the perigee for the orbital trajectories around the binary asteroid system.

A comparison of the variations in the ascending node declination and near-asteroid amplitude angle between the orbits of the ABCD and EFGH groups revealed distinct patterns. Notably, in the vertical orbit group, group C showed the most significant change in ascending node decline, whereas in the horizontal orbit group, this change was most pronounced in group H. These results align with the results of earlier analyses, suggesting that the larger variation in group C may be because of its closer proximity to the companion asteroid, which could result in a more noticeable change in the ascending node declination compared with that in group D. However, more research is needed to determine the exact cause. Additionally, both the horizontal and vertical groups exhibited periodic fluctuations in the ascending node longitude; however, the extent of these variations differed significantly. For instance, the vertical ABCD group shows a range from 3.6 to 4.1 radians, whereas the horizontal EFGH group has a broader range from 0 to 6.3 radians, with the FGH group exceeding 6.3 radians. This difference highlights the critical influence of proximity on the dynamics of the FGH group, reinforcing the idea that the vertical orbit group maintains a more stable trajectory than does the horizontal group.

The perigee angle consistently increased from 0 for both the horizontal and vertical orbit groups. Notably, in the vertical orbit group, the perigee angle change in the CD group, which had a smaller orbital radius, was significantly faster than that in the AB group. Similarly, in the horizontal orbit group, the H group, which had the smallest orbital

radius, showed the fastest increase in the perigee angle. Although the rates of increase in the perigee angle differed between the two groups, their response patterns remained consistent. Specifically, the closer the probe orbit was to the primary asteroid, the faster the perigee angle increased. This trend was observed across both the horizontal and vertical orbit groups.

4.3. Analysis of Detector Solar Pressure

The effect of solar pressure on the weak gravitational field systems of asteroids is indeed worth considering. Since the solar pressure is affected by the spacecraft illumination area and the variation in the light pressure coefficients of different material surfaces, it is difficult to model it accurately; for this kind of modelling error, it is usually compensated by estimating the model coefficients during the orbit fixing process. In other words, a fixed surface-to-mass ratio model is used to model the solar pressure received by the spacecraft. The photopressure generated by sunlight on an object in Earth orbit is about 5×10^{-6} N/m^2, and this value is based on measurements when sunlight is directed onto a black ground (100% absorption). Due to the weak gravitational field of the asteroid, the effect of solar light pressure on spacecraft for deep space exploration is often non-negligible. This is particularly true for the binary asteroid of 1999 KW4, which has a high orbital eccentricity and is approximately 30 million km away from the Sun at the beginning of the closest time. At that time, it is closer to the Sun than Mercury, with a solar light pressure of 2.5×10^{-5} N/m^2. Considering that the spacecraft is not an ideal black body, the estimated model coefficient can be used to take the area of 4 m $\times$ 1 m as the reflective area, and the total reflective efficiency is set to 60%, which in turn can be used to find out the solar pressure on the spacecraft at this time and then add it to the model calculation to obtain the following comparative chart of orbit results:

As illustrated in Figure 10. Using the group E orbits as an example, the left figure depicts the result without considering light pressure, while the right figure shows the result after incorporating solar light pressure. It is evident that there is minimal disparity between the two orbits. To conduct a thorough comparison, it is essential to analyze and compare the X-direction coordinates and velocities of the orbits obtained from both calculations.

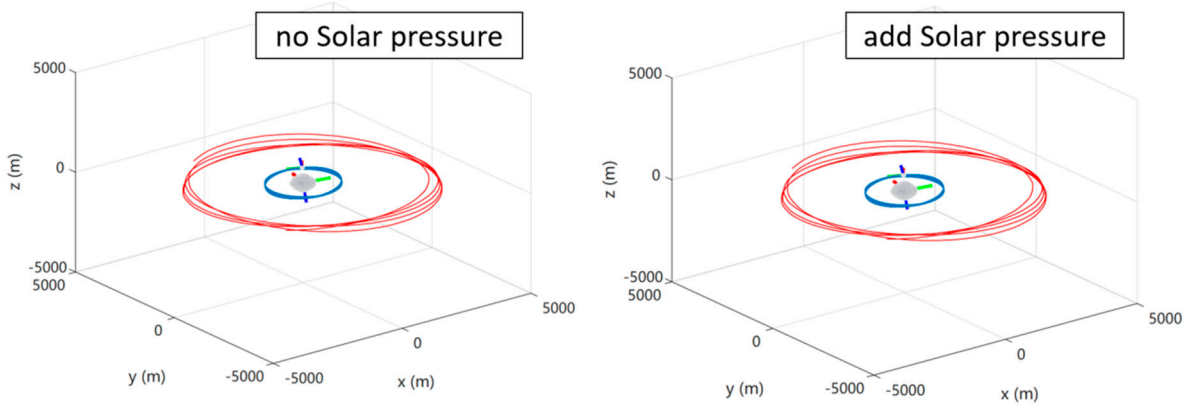

Figure 10. Comparison of detector orbits after adding solar pressure.

As illustrated in Figure 11. A comparison of the aforementioned figure reveals that, after accounting for the effects of solar pressure, the orbit's displacement deviation remains at 0.4 m after ten days of simulation, while the velocity deviation is reduced to 0.08 cm/s. The relatively minor influence of solar pressure on satellite orbits is likely due to our simulation, which assumes that the detector does not possess a solar sail structure. The detector's solar pressure is still an order of magnitude lower than the gravitational force exerted on it by the asteroid. Consequently, the resulting orbit deviation is not significant over a short time frame. The solar pressure on an ordinary probe also remains less than the gravitational force exerted by an asteroid on it, exhibiting an order of magnitude difference

and resulting in insignificant orbit deviation over a short period. However, for long-term observation of an asteroid system, solar pressure accumulation will necessitate active orbital control to maintain stability.

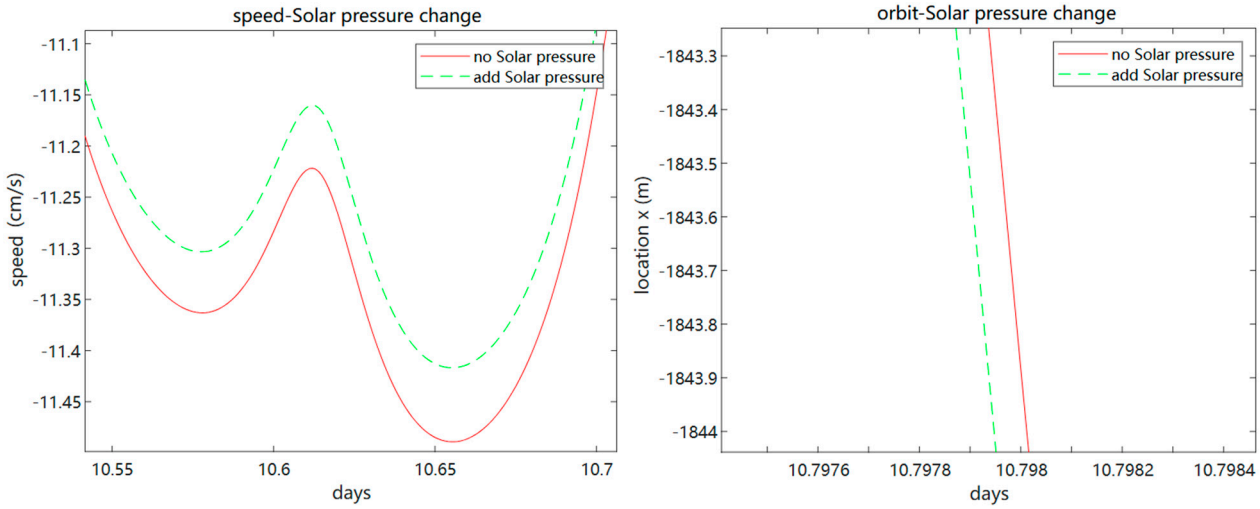

Figure 11. Comparison of detector velocity and displacement after adding solar pressure.

5. Analysis of the Orbital Stability of Double Asteroid System Probe

5.1. Introduction

When assessing track stability, it is inevitable to encounter ambiguity and randomness in the evaluation indexes and data. However, the cloud model serves as a natural language representation that can effectively translate uncertainty between qualitative concepts and quantitative values, fully accounting for the ambiguity and randomness inherent in the evaluation process. This paper aims to apply the normal cloud model to the hierarchical prediction of track stability, thereby introducing a new method and idea for the hierarchical prediction of track stability.

5.2. Cloud Concepts and Digital Features

The cloud model is a conceptual framework that addresses the inherent ambiguity and randomness associated with the transformation between qualitative concepts and quantitative descriptions. It facilitates the integration of these disparate elements within the context of spatial data mining, establishing a mutual mapping relationship between qualitative and quantitative. The cloud model comprises three numerical features: the expected value (*Ex*), entropy (*En*), and hyperentropy (*He*). The expected value (*Ex*) represents the point value of qualitative concepts; the entropy (*En*) represents the degree of vagueness; and the hyperentropy (*He*) represents the entropy of entropy, i.e., the uncertainty of vagueness. The cloud model has been successfully applied in a number of fields, including natural language processing, data mining, decision analysis, intelligent control, and image processing.

5.3. Construction of the Evaluation Indicator System

A plethora of characterization data is available for the evaluation of orbital stability, categorized by each group of orbits. As the gravitational field of the double asteroid system under the finite element model is a time-varying system, it is significantly influenced by a number of factors, including the initial position state of the double asteroid, the physical structural characteristics of the asteroid, the orbiting speed and position, and others. In consideration of the impact of each factor on the detector's orbit stability, it was ultimately determined that the orbit half-length axis, eccentricity, and variance of the orbit inclination would serve as the evaluation indices for orbit stability. The relationship between the orbit stability and the aforementioned evaluation indices is illustrated in Table 4.

Table 4. The initial conditions of the detector on each orbit.

Stable Category	Standard Deviation of Half-Length Axis	Standard Deviation of Eccentricity	Standard Deviation of Track Inclination
I (excellent)	<200	<0.5	<0.01
II (good)	200–400	0.5–0.6	0.01–0.02
III (fair)	400–600	0.6–0.7	0.02–0.03
IV (poor)	600–800	0.7–0.8	0.03–0.04
V (bad)	>800	>0.8	>0.04
Individual indicator weights	0.16	0.3	0.54

5.4. Numerical Characterization of Cloud Models of Orbital Stability

The definition of the normal cloud model reveals that we can calculate the cloud numerical characteristics of the track stability evaluation factor for a specific class criterion using the following formula:

$$E_x = \frac{C_{\min} + C_{\max}}{2} \tag{20}$$

$$E_n = \frac{C_{\max} - C_{\min}}{6} \tag{21}$$

$$H_e = k \tag{22}$$

In the aforementioned equation, $C_{\max}$ and $C_{\min}$ represent the maximum and minimum boundaries of a specific level of criteria, respectively. For a given variable with unilateral boundaries, the boundary parameter can be determined based on the upper and lower limits of the data. The variable's fuzzy threshold can adjust k, a constant that is typically set to 0.01. The numerical characteristics of the various stabilization levels are illustrated in Table 5:

Table 5. The initial conditions of the detector on each orbit.

Stabilization Level	Digital Identity	Standard Deviation of Half-Length Axis	Standard Deviation of Eccentricity	Standard Deviation of Track Inclination
I (excellent)	Ex	100	0.45	0.005
	En	33.33	0.017	0.0017
	He	0.01	0.01	0.01
II (good)	Ex	300	0.55	0.015
	En	33.33	0.017	0.0017
	He	0.01	0.01	0.01
III (fair)	Ex	500	0.65	0.025
	En	33.33	0.017	0.0017
	He	0.01	0.01	0.01
IV (poor)	Ex	700	0.75	0.035
	En	33.33	0.017	0.0017
	He	0.01	0.01	0.01
V (bad)	Ex	900	0.85	0.045
	En	33.33	0.017	0.0017
	He	0.01	0.01	0.01

5.5. Determination of Weighting Factors Based on Hierarchical Analysis Approach

Weights serve to characterize the relative importance of each track stability index, indicating the different roles that each evaluation index plays in the overall system. Currently, a variety of methods exist for calculating the weights, including the weighted average method, hierarchical analysis method, Delphi method, and principal component analys. In this paper, we utilized a simple and practical hierarchical analysis method to calculate the weights, setting the analytical value of the three as 1:2:3. We conducted this by comprehensively considering the relative importance of the standard deviation of the half-length axis, the standard deviation of the eccentricity rate, and the standard deviation of the track inclination angle, and combining the importance of their differences in the track's stability. After normalization and consistency testing, we constructed a hierarchical analysis matrix and calculate the index weights, respectively.

5.6. Generation of Cloud Models for Orbital Stability Indicators

Based on the theory of the normal cloud model, the cloud model parameters Ex, En, and He were determined, and the forward cloud generator was used to generate the corresponding cloud model for the evaluation factors: standard deviation of the half-length axis, standard deviation of eccentricity, and standard deviation of track inclination, as shown in Figure 12. The horizontal coordinate represents the value of each evaluation index, while the vertical coordinate represents the corresponding degree of certainty. In Figure 12, from right to left, the standard evaluation clouds corresponding to the stability indicators of level I to level V orbits are represented.

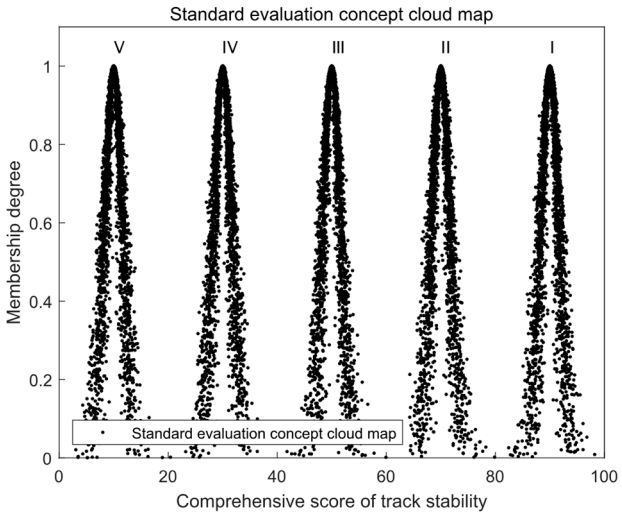

Figure 12. Comparison of the detector velocity and displacement after adding solar pressure.

5.7. Model Test Results for Each Orbit Group

Table 6 shows the rating of orbital stability that was obtained using the hierarchical analysis-normal cloud model and how it compares to the qualitative analysis that was discussed earlier. As can be seen from the table, the results of the hierarchical analysis-normal cloud model are the same as those of the qualitative analysis, and groups A, E, and F, whose orbits are farther away from the binary asteroid, show better ratings, while group B, whose orbits are closer to the companion asteroid for a longer period of time, suffers from a greatly reduced perturbation of orbital stability rating. This demonstrates the high reliability of the orbital stability prediction model based on the hierarchical analysis method (normal cloud) and also confirms the model's feasibility and validity for the orbital stability assessment of other probes with similar binary asteroid systems.

By using the standard evaluation concept cloud map, the stability evaluation results of these sets of orbital data can be more intuitively displayed. The stability evaluation cloud maps of the ABCD group and EFGH group are shown in Figures 13 and 14.

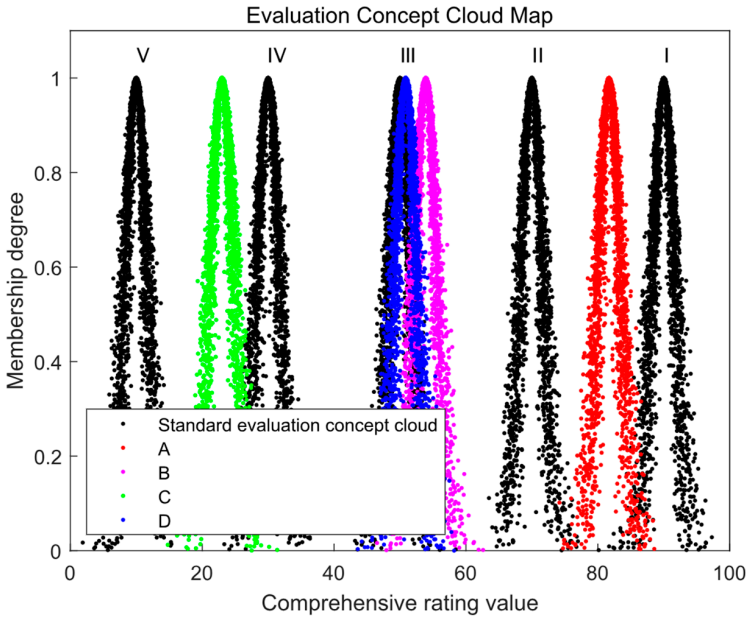

Figure 13. ABCD group orbit stability membership cloud map.

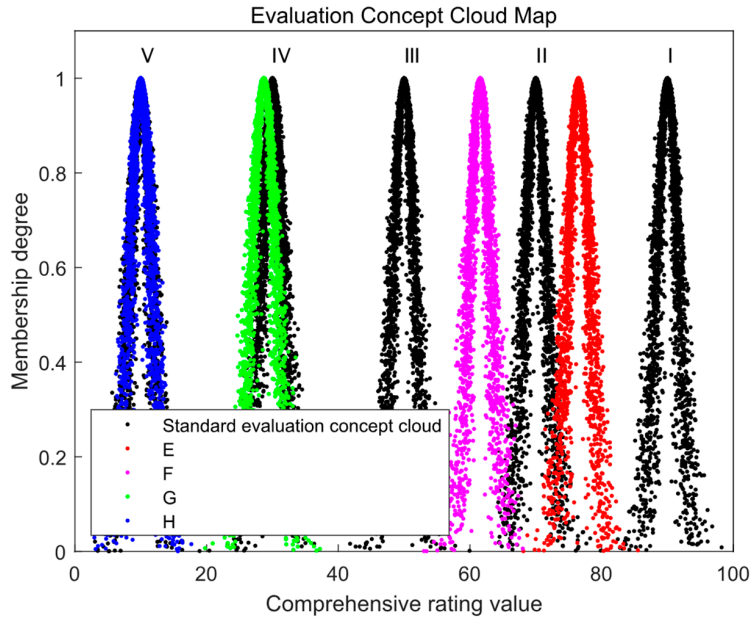

Figure 14. EFGH group orbit stability membership cloud map.

Table 6. The initial conditions of the detector on each orbit.

Experimental Data Sets	Standard Deviation of Half-Length Axis	Standard Deviation of Eccentricity	Standard Deviation of Track Inclination	Rating Level
A	296.5	0.5102	0.007099	I
B	465.6	0.7863	0.009105	III
C	969.6	1.099	0.03897	IV
D	456.4	0.9693	0.02043	III
E	164.1	0.4051	0.01845	II
F	246.9	0.5600	0.02729	II
G	363.6	0.8238	0.03424	IV
H	2361	1.819	0.08169	V

6. Conclusions

This study uses the finite element method to simulate the motion trajectories of binary asteroid systems and analyze the orbit of a probe. This method calculates the interaction forces between binary asteroids to determine their motion trajectories. These trajectories were then validated against the observed motion of the 1999 KW4 binary asteroid system to demonstrate the reliability of the finite element approach for modeling binary asteroids.

Using this approach, we can analyze probe orbits within binary systems. Introducing probe orbits adds complexity to the dynamic structure because of non-spherical gravitational effects, the time-varying nature of binary systems, and resonance effects from the orbit of the companion asteroid. This study examined two types of orbits and reached consistent findings: stable probe orbits occur only when the semi-major axis is more than 1000 m from the orbit of the companion asteroid. Orbits that are too close to the companion asteroid show significant instability within 10 cycles, and they are marked by longer orbital periods, increased orbital radii, and quicker changes in parameters, all of which can lead to complete orbital instability.

The further analysis of the semi-major axis, eccentricity, orbital inclination, longitude of the ascending node, near-asteroid amplitude angle, and velocity of orbits in the horizontal and vertical groups revealed that vertical orbits generally showed more stable variations in parameters such as the semi-major axis, velocity, eccentricity, and near-asteroid amplitude angle. Although these parameters still exhibited periodic fluctuations, the extent of the variation in the vertical group was relatively small. In contrast, the orbital inclination in the horizontal group, while trending upward, displayed smaller local fluctuations, indicating a greater stability. In contrast, the longitude of the ascending node in the vertical group exhibited larger fluctuations and a rapid downward trend. Additionally, close encounters with the companion asteroid significantly disrupted the orbit of the probe, highlighting a major impact that cannot be ignored.

Considering the characteristics of the weak gravity field of asteroids, a solar pressure analysis was introduced, and it was found that the influence of solar pressure on the probe's orbit was not significant during the ten-day simulation time. In order to quantitatively analyze the stability characteristics of each group's orbit more scientifically, a cloud model evaluation method was introduced. Based on this, parameters characterizing the stability of each group's orbit were selected, and the stability results of the ABCD and EFGH groups' orbits were more intuitively displayed by drawing a cloud model evaluation chart. The conclusion is consistent with the qualitative analysis in the previous section.

In future research, the proposed methodology can be applied to the design of landing orbits for probes targeting similar binary asteroid systems. New techniques can be developed to create probe orbits by incorporating the latest advancements in artificial intelligence, including machine learning and generative AI [27–29]. Such integration would enhance efficiency and increase the amount of information that could be extracted from these systems.

Author Contributions: Methodology, L.S.; Software, L.Y.; Formal analysis, M.H.; Investigation, M.H.; Resources, Z.F.; Data curation, W.F. and Z.F.; Writing—original draft, L.S.; Writing—review & editing, L.S.; Funding acquisition, N.Q. All authors have read and agreed to the published version of the manuscript.

Funding: This work was supported in part by the National Natural Science Foundation of China (grant number U23B6001) and in part by the National Natural Science Foundation of China (grant number U22B2013).

Data Availability Statement: The original contributions presented in the study are included in the article, further inquiries can be directed to the corresponding author.

Conflicts of Interest: The authors declare no conflict of interest.

References

1. Levison, H.F.; Olkin, C.; Noll, K.S.; Marchi, S.; Team, L. Lucy: Surveying the diversity of the trojan asteroids: The fossils of planet formation. In Proceedings of the 48th Lunar and Planetary Science Conference, Woodlands, TX, USA, 20–24 March 2017.
2. Cheng, A.F.; Michel, P.; Barnouin, O.S.; Campo-Bagatin, A.; Miller, P.; Pravec, P.; Richardson, D.C.; Rivkin, A.S.; Schwartz, S.R.; Stickel, A.; et al. Asteroid Impact and Deflection Assessment (AIDA) mission: The Double Asteroid Redirection Test (DART). In Proceedings of the 47th Lunar and Planetary Science Conference, Woodlands, YX, USA, 21–25 March 2016.
3. Scheeres, D.J.; McMahon, J.W.; Bierhaus, E.B.; Wood, J.; Benner, L.A.; Hartzell, C.M.; Hayne, P.; Jedicke, R.; Le Corre, L.; Meyer, A.; et al. Janus: A NASA Simplex mission to explore two NEO binary asteroids. In Proceedings of the 51st Lunar and Planetary Science Conference, Woodlands, TX, USA, 16–20 March 2020.
4. Merline, W.J.; Weidenschilling, S.J.; Durda, D.D.; Margot, J.L.; Pravec, P.; Storrs, A.D. Asteroids do have satellites. In *Tuscon Arizona: Asteroids III*; University of Arizona Press: Tucson, AZ, USA, 2002; pp. 289–312.
5. Werner, R.A.; Scheeres, D.J. Mutual potential of homogeneous polyhedra. *Celest. Mech. Dyn. Astron.* **2005**, *91*, 337–349. [CrossRef]
6. Scheeres, D.J.; Fahnestock, E.G.; Ostro, S.J.; Margot, J.L.; Benner, L.A.; Broschart, S.B.; Bellerose, J.; Giorgini, J.D.; Nolan, M.C.; Magri, C.; et al. Dynamical configuration of binary near-Earth asteroid (66391) 1999 KW4. *Science* **2006**, *314*, 1280–1283. [CrossRef]
7. Fahnestock, E.G.; Scheeres, D.J. Simulation and analysis of the dynamics of binary near-Earth asteroid (66391) 1999 KW4. *Icarus* **2008**, *194*, 410–435. [CrossRef]
8. Compère, A.; Lemaitre, A. The two-body interaction potential in the STF tensor formalism: An application to binary asteroids. *J. Celest. Mech. Dyn. Astron.* **2014**, *119*, 313–330. [CrossRef]
9. Shi, Y.; Wang, Y.; Xu, S. Mutual gravitational potential, force, and torque of a homogeneous polyhedron and an extended body: An application to binary asteroids. *J. Celestial Mech. Dyn. Astron.* **2017**, *129*, 307–320. [CrossRef]
10. Yu, Y.; Cheng, B.; Hayabayashi, M.; Michel, P.; Baoyin, H. A finite element method for computational full two-body problem: I. The mutual potential and derivatives over bilinear tetrahedron elements. *Celest. Mech. Dyn. Astron.* **2019**, *131*, 51. [CrossRef]
11. Damme, F.; Hussmann, H.; Oberst, J. Spacecraft orbit lifetime within two binary near-Earth asteroid systems. *Planet. Space Sci.* **2017**, *146*, 1–9. [CrossRef]
12. Dell'Elce, L.; Baresi, N.; Naidu, S.P.; Benner, L.A.; Scheeres, D.J. Numerical investigation of the dynamical environment of 65803 Didymos. *Adv. Space Res.* **2017**, *59*, 1304–1320. [CrossRef]
13. Shang, H.; Wu, X.; Cui, P. Trajectory exploration within asynchronous binary asteroid systems using refined Lagrangian coherent structures. *Celest. Mech. Dynam. Astronom.* **2017**, *127*, 185–210. [CrossRef]
14. Ferrari, F.; Franzese, V.; Pugliatti, M.; Giordano, C.; Topputo, F. Trajectory options for Hera's Milani CubeSat around (65803) didymos. *J. Astronaut. Sci.* **2021**, *68*, 973–994. [CrossRef]
15. Naidu, S.P.; Benner, L.A.; Brozovic, M.; Nolan, M.C.; Ostro, S.J.; Margot, J.L.; Giorgini, J.D.; Hirabayashi, T.; Scheeres, D.J.; Pravec, P.; et al. Radar observations and a physical model of binary near-Earth asteroid 65803 Didymos, target of the DART mission. *Icarus* **2020**, *348*, 113777. [CrossRef]
16. Takei, Y.; Saiki, T.; Yamamoto, Y.; Mimasu, Y.; Takeuchi, H.; Ikeda, H.; Ogawa, N.; Terui, F.; Ono, G.; Yoshikawa, K.; et al. Hayabusa2's station-keeping operation in the proximity of the asteroid Ryugu. *Astrodynamics* **2020**, *4*, 349–375. [CrossRef]
17. Yin, W.; Shi, Y.; Shu, L.; Gao, Y. Autonomous navigation of an asteroid orbiter enhanced by a beacon satellite in a high-altitude orbit. *Astrodynamics* **2024**, *8*, 375–400. [CrossRef]
18. Wen, T.; Zeng, X.; Li, Z.; Yu, Y. A comparative assessment of gravitational field modeling methods for binary asteroid landing. *Astrodynamics* **2024**, *8*, 417–435. [CrossRef]
19. Chen, H. Capacity of Sun-driven lunar swingby sequences and their application in asteroid retrieval. *Astrodynamics* **2023**, *7*, 315–334. [CrossRef]
20. Balhareth, G.; Ilyas, M. Optimized Intrusion Detection for IoMT Networks with Tree-Based Machine Learning and Filter-Based Feature Selection. *Sensors* **2024**, *24*, 5712. [CrossRef] [PubMed]
21. Zhang, J.; Shen, D. GPU-Based Implementation of Finite Element Method for Elasticity Using Cuda. In Proceedings of the 2013 IEEE 10th International Conference on High Performance Computing and Communications & 2013 IEEE International Conference on Embedded and Ubiquitous Computing 2013, Zhangjiajie, China, 13–15 November 2013; pp. 1003–1008. [CrossRef]
22. Zhang, Y.H.; Qian, Y.J.; Li, X.; Yang, X.D. Resonant orbit search and stability analysis for elongated asteroids. *Astrodynamics* **2023**, *7*, 51–67. [CrossRef]
23. Chu, Y.; Baoyin, H.; Gong, S. Dynamics and control of sun-facing diffractive solar sails in displaced orbit for asteroid deflection. *Aerosp. Sci. Technol.* **2024**, *145*, 165–175. [CrossRef]
24. Yu, Z.; Shang, H.; Wei, B. Accessibility assessment and trajectory design for multiple Near-Earth-asteroids exploration using stand-alone CubeSats. *Aerosp. Sci. Technol.* **2019**, *95*, 105–477.
25. Bertolucci, G.; Barato, F.; Toson, E.; Pavarin, D. Impact of propulsion system characteristics on the potential for cost reduction of earth observation missions at very low altitudes. *Acta Astronaut.* **2020**, *176*, 173–191. [CrossRef]
26. Pontani, M.; Teofilatto, P. Deployment strategies of a satellite constellation for polar ice monitoring. *Acta Astronaut.* **2022**, *193*, 346–356. [CrossRef]
27. Muralidharan, V.; Makhdoomi, M.R.; Barad, K.R.; Amaya-Mejía, L.M.; Howell, K.C.; Olivares-Mendez, M. Rendezvous in cislunar halo orbits: Hardwarein-the-loop simulation with coupled orbit and attitude dynamics. *Acta Astronaut.* **2023**, *211*, 556–573. [CrossRef]

28. Trofimov, S.; Shirobokov, M.; Tselousova, A.; Ovchinnikov, M. Transfers from near-rectilinear halo orbits to low-perilune orbits and the Moon's surface. *Acta Astronaut.* **2020**, *167*, 260–271. [CrossRef]
29. Pontani, M.; Celani, F. Variable-time-domain neighboring optimal guidance and attitude control of low-thrust lunar orbit transfers. *Acta Astronaut.* **2020**, *175*, 616–626. [CrossRef]

Disclaimer/Publisher's Note: The statements, opinions and data contained in all publications are solely those of the individual author(s) and contributor(s) and not of MDPI and/or the editor(s). MDPI and/or the editor(s) disclaim responsibility for any injury to people or property resulting from any ideas, methods, instructions or products referred to in the content.